

Transport across junctions of a Weyl and a multi-Weyl semimetal

Debabrata Sinha and K. Sengupta

*School of Physical Sciences, Indian Association for the Cultivation of Science,
2A and 2B Raja S.C. Mullick Road, Jadavpur-700032, India.*

(Dated: February 26, 2019)

We study transport across junctions of a Weyl and a multi-Weyl semimetal (WSM and a MSM) separated by a region of thickness d which has a barrier potential U_0 . We show that in the thin barrier limit ($U_0 \rightarrow \infty$ and $d \rightarrow 0$ with $\chi = U_0 d / (\hbar v_F)$ kept finite, where v_F is velocity of low-energy electrons and \hbar is Planck's constant), the tunneling conductance G across such a junction becomes independent of χ . We demonstrate that such a barrier independence is a consequence of the change in the topological winding number of the Weyl nodes across the junction and point out that it has no analogue in tunneling conductance of either junctions of two-dimensional topological materials (such as graphene or topological insulators) or those made out of WSMs or MSMs with same topological winding numbers. We study this phenomenon both for normal-barrier-normal (NBN) and normal-barrier-superconductor (NBS) junctions involving WSMs and MSMs with arbitrary winding numbers and discuss experiments which can test our theory.

PACS numbers:

I. INTRODUCTION

A Weyl semimetal (WSM) hosts a three-dimensional (3D) gapless topological state whose wavefunction carries a non-zero topological winding number arising out of singularity in \mathbf{k} space^{1–4}. These singularities occur at Weyl points where the conduction and the valence bands touch. The low-energy effective Hamiltonian of these WSMs around these Weyl points is given by $H = \pm \hbar v_F \vec{\tau} \cdot \vec{k}$, where $\vec{k} = (k_x, k_y, k_z)$ is the wave vector, v_F is the velocity of the electrons near the Weyl point which depends on material parameters, and $\vec{\tau}$ denotes Pauli matrices. These Weyl nodes occur in pairs and are protected due to either time-reversal or inversion symmetry breaking¹. Such isotropic Weyl nodes are characterized by a topological winding number which takes values ± 1 depending on the chirality of the electrons around the node. The electron around such nodes display spin momentum locking; this property along with the linear dispersion $E_{\vec{k}} = \pm \hbar v_F |\vec{k}|$ and a non-zero topological winding number distinguishes WSMs from ordinary metals. This distinction is manifested in several unconventional features associated with transport, magneto-transport and edge physics of these materials^{1,5–8}.

More recently, materials with Weyl points having anisotropic dispersion in two transverse direction (chosen to be k_x and k_y in this work) has been discovered⁹. Such materials are termed as multi-Weyl semimetals (MSMs) since their anisotropic dispersion occurs due to merger of two or more Weyl nodes with same chirality. Such a merger is found to be topologically protected by point group symmetries (such as C_4 and C_6 rotational symmetries)¹⁰. The low energy dispersion of the electrons in MSMs remain linear in the symmetry direction (chosen to be k_z in this work) but vanishes as k^n (where $k = \sqrt{k_x^2 + k_y^2}$) with $n > 1$ in the transverse directions: $E(k_z = 0, k) \sim k^n$ [9–11]. The topological winding num-

ber of these anisotropic Weyl points is given by an integer n with $n \leq 3$ [10]. The presence of a winding number different from unity modifies the helicity properties and the density of states of the electrons in these materials¹². Several other signatures of $n \neq 1$ show up in optical and transport quantities such as longitudinal optical conductivity, anomalous Hall conductivity, collective modes, and magnetoresistance^{13–15}.

It is well known that transport measurement across junctions of topological materials provides access to their topological properties and unravels several unconventional features that have no analog in standard metals^{16–21}. In 2D topological materials such as graphene, the tunneling conductance G across graphene normal metal-barrier-normal metal (NBN) junctions, display oscillatory behavior and a transmission resonance as a function of the barrier potential¹⁶. Similar behavior is also seen in subgap tunneling conductance of graphene NBS junctions, where superconductivity is induced in graphene via a proximate s -wave superconductor¹⁸. Such an oscillatory behavior and the transmission resonance phenomenon turns out to be a signature of the Dirac quasiparticles in graphene; they do not occur in standard metals with Schrodinger quasiparticles in the regime where the incident energy of a quasiparticle is small compared to the barrier height. Similar behavior is also seen for quasiparticles on the surface of a topological insulator¹⁹. More recently tunneling conductance across NBN and NBS junctions of WSMs have also been studied^{21–24}. In particular, it was found that the NBS junctions of time-reversal symmetric Weyl semimetals may host a universal zero-bias conductance value of e^2/h . In addition, the subgap tunneling conductance is found to oscillate as a function of the barrier strength as expected for standard Dirac materials²³.

In this work, we study the tunneling conductance across NBN and NBS junctions between either a WSM ($n = 1$) and a MSM ($n \neq 1$) or two MSMs with $n_1 \neq n_2$

separated by a barrier of width d and a potential U_0 . Such junctions differ from their previously studied WSM counterparts in the sense that the topological winding number of the system changes across these junctions. The main results obtained from our study are as follows. First, we show that the tunneling conductance G of these junctions becomes independent of the barrier potential in the thin barrier limit where $U_0 \rightarrow \infty$ and $d \rightarrow 0$ with $\chi = U_0 d / (\hbar v_F)$ being held fixed. We note that this behavior is in contrast to that found in junctions of both ordinary Schrodinger metals (where G is a monotonically decaying function of χ) and Dirac or WSM materials (where G oscillates with χ). We demonstrate that this independence is a consequence of difference of winding numbers between the WSM and MSM (or two MSMs) on two sides of the junction. Second, we find that the subgap tunneling conductance of the NBS junction depends crucially on the topological winding numbers. It vanishes if superconductivity is induced on the MSM with higher topological winding number; in contrast, it is finite when superconductivity is induced on the WSM or MSM with lower topological winding number. Third, we analyze the fate of the tunneling conductance G for these junctions away from the thin barrier limit. We find that they display weak oscillatory dependence on the barrier potential U_0 for finite barrier thickness d ; the amplitude (period) of these oscillations decreases (increases) with d for any finite U_0 . For large U_0 , G becomes independent of U_0 leading to the thin barrier result. Finally, we discuss experiments which can test our theory.

The plan of the rest of the paper is as follows. In Sec. II, we analyze the transport in NBN junctions between a WSM and a MSM or two MSMs with different winding numbers. This is followed by a similar analysis for NBS junctions in Sec. III. Finally, we discuss our main results, point out relevant experiments which may test our theory, and conclude in Sec. IV. We detail some of the calculation regarding inter-node scattering in the Appendix.

II. NBN JUNCTIONS

In this section we shall derive the conductance of a NBN junction between a WSM and a MSM or two MSMs with different winding numbers. The geometry of the setup is sketched in Fig. 1. The Hamiltonian of the system is given by

$$H = H_1 \theta(d - z) + U_0 \theta(d - z) \theta(z) + H_2 \theta(z - d) \quad (1)$$

where $\theta(z)$ is the Heaviside step function. The Hamiltonians H_1 and H_2 are given by

$$\begin{aligned} H_1 &= E_0(-i\partial_z\tau_z + \epsilon_0 k^{n_1} \\ &\quad \times [\cos(n_1\phi_k)\tau_x + \tau_y \sin(n_1\phi_k)]) \\ H_2 &= \eta^{-1} E_0(-i\partial_z\tau_z + \epsilon'_0 k^{n_2} \\ &\quad \times [\cos(n_2\phi_k)\tau_x + \tau_y \sin(n_2\phi_k)]), \end{aligned} \quad (2)$$

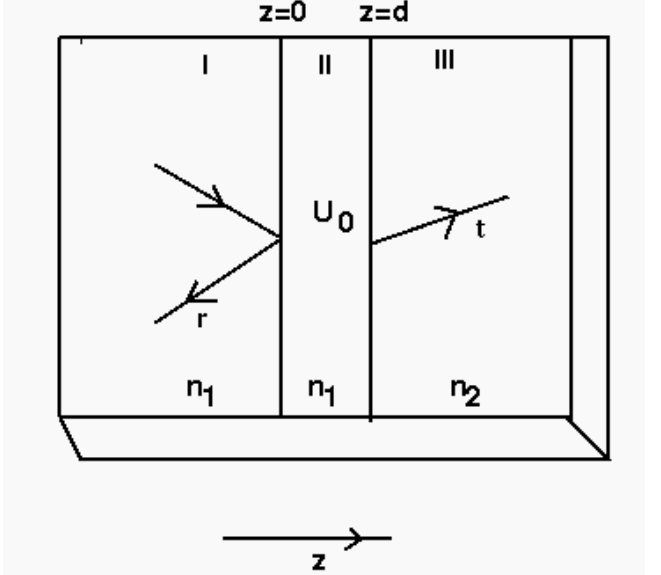


FIG. 1: A schemetaic representation of a junction between two MSMs or a WSM and a MSM (characterized by topological winding numbers n_1 and n_2 as shown) in regions I and III separated by a barrier in region II. The barrier region II extending from $z = 0$ to $z = d$ constitutes the same material as in region I but has an additional potential U_0 . The reflection and transmission amplitudes, r and t , for an electron approaching the barrier from region I is shown schematically.

where n_1 and n_2 are the topological winding numbers in regions I and III as shown in Fig. 1, $\phi_k = \arctan(k_y/k_x)$, and $E_0 = \hbar v_F k_0$ is the energy scale in which all energies are measured. In the rest of this work, we shall take this energy scale to be upper cutoff up to which the low-energy continuum Hamiltonians (Eq. 2) hold. Here v_F and $v'_F = v_F/\eta$ are the Fermi velocities for electrons in region I and III, k_0 is the momentum scale chosen to make all momenta dimensionless, and ϵ_0 and ϵ'_0 are material specific constants whose precise numerical value is not going to alter our main results. We shall further choose a common chemical potential μ_N across the junction. We note that the analysis we carry out holds even if the chemical potentials in regions I and III are different; we nevertheless choose them to be the same to reduce the number of parameters in the theory. Moreover it is always possible to align the chemical potentials in regions I and III by applying a voltage across one of them. In what follows, we shall apply a voltage V across the junction and compute G as a function of V .

To compute G , we first consider the electron wavefunction in region I. A straightforward calculation shows that the wavefunction for right(R) and left(L) moving electrons in region I in the presence of an applied voltage

eV is given by²³

$$\begin{aligned}\psi_{1eR} &= e^{i(k_x x + k_y y + k_z z)} e^{-i\tau_z n_1 \phi_k / 2} (\cos(\theta_1), \sin(\theta_1))^T \\ \psi_{1eL} &= e^{i(k_x x + k_y y - k_z z)} e^{-i\tau_z n_1 \phi_k / 2} (\sin(\theta_1), \cos(\theta_1))^T\end{aligned}\quad (3)$$

where $2\theta_1 = \arcsin(\epsilon_0 k^{n_1} / |eV + \mu_N|)$, $k = \sqrt{k_x^2 + k_y^2}$, $k_{z1} = \text{Sgn}(eV + \mu_N + \epsilon_0 k^{n_1}) \sqrt{(eV + \mu_N)^2 - \epsilon_0^2 k^{2n_1}}$ and we have measured all energies (wavevectors) in units of $E_0 = \hbar v_F k_0$ (k_0). We note that here and in the rest of this work, the temporal dependence of the wavefunctions [*i.e.* $\exp[-i(eV)t/\hbar]$ factor] has not been explicitly mentioned for clarity.

The wavefunction in region I can be written in terms of ψ_{eR} and ψ_{eL} as

$$\psi_1 = \psi_{1eR} + r\psi_{1eL} \quad (4)$$

where r is the amplitude of reflection from the barrier. We note here that $\psi_{1eR(L)} \sim e^{-i\tau_z n_1 \phi_k / 2}$ leading to $\psi_1 \sim e^{-i\tau_z n_1 \phi_k / 2}$; thus the azimuthal angle dependence of the wavefunction in region I can be interpreted as a spin rotation by an angle of $n_1 \phi_k$ about the \hat{z} axis.

In region II, the electrons see an additional applied potential U_0 . The right and the left moving electron wavefunction in this regime can be written as

$$\begin{aligned}\psi_{2eR} &= e^{i(k_x x + k_y y + k_z z)} e^{-i\tau_z n_1 \phi_k / 2} (\cos(\theta_2), \sin(\theta_2))^T \\ \psi_{2eL} &= e^{i(k_x x + k_y y - k_z z)} e^{-i\tau_z n_1 \phi_k / 2} (\sin(\theta_2), \cos(\theta_2))^T\end{aligned}\quad (5)$$

where $k_{z2} = \text{Sgn}(eV + \mu_N - U_0 + \epsilon_0 k^{n_1}) \sqrt{(eV + \mu_N - U_0)^2 - \epsilon_0^2 k^{2n_1}}$ and $2\theta_2 = \arcsin(\epsilon_0 k^{n_1} / |eV + \mu_N - U_0|)$. We note that $\theta_2 \rightarrow 0$ when $U_0 \rightarrow \infty$. Thus the wavefunction in region II can

be written as

$$\psi_{II} = p\psi_{2eR} + q\psi_{2eL} \quad (6)$$

where p and q denotes amplitudes of right and left moving electrons in region II. We note that θ_2 and θ_1 are related by

$$\theta_2 = \frac{1}{2} \arcsin[\sin(2\theta_1) / |1 - U_0 / (eV + \mu_N)|] \quad (7)$$

In region III, the right moving electrons have a wavefunction given by

$$\psi_{3eR} = e^{i(k_x x + k_y y + k_z z)} e^{-i\tau_z n_2 \phi_k / 2} (\cos(\theta_3), \sin(\theta_3))^T \quad (8)$$

where $2\theta_3 = \arcsin(\epsilon_0' k^{n_2} / |\eta(eV + \mu_N)|)$, $k_{z3} = \text{Sgn}[(eV + \mu_N)\eta + \epsilon_0' k^{n_2}] \sqrt{(eV + \mu_N)^2 \eta^2 - \epsilon_0'^2 k^{2n_2}}$, and η is the measure of the Fermi velocity mismatch across the junction. We note that θ_1 and θ_3 , for any given voltage eV , are related by

$$\sin(2\theta_3) = |eV + \mu_N|^{n_2/n_1-1} \sin[2\theta_1]^{n_2/n_1} \frac{\epsilon_0'}{\eta \epsilon_0^{n_2/n_1}} \quad (9)$$

The wavefunction in region III is thus given by

$$\psi_{III} = t\psi_{3eR} \quad (10)$$

where t is the transmission amplitude across the junction. We note that $\psi_3 \sim e^{-i\tau_z n_2 \phi_k / 2}$.

To obtain the reflection and transmission amplitude across the barrier, we match the wavefunctions at $z = 0$ and $z = d$, where $d \equiv dk_0$ constitutes the width of the barrier in units of k_0^{-1} . This requires $\psi_I(z = 0) = \psi_{II}(z = 0)$ and $\psi_{II}(z = d) = \psi_{III}(z = d)$ and leads to

$$\begin{aligned}\cos(\theta_1) + r \sin(\theta_1) &= p \cos(\theta_2) + q \sin(\theta_2) \\ \sin(\theta_1) + r \cos(\theta_1) &= p \sin(\theta_2) + q \cos(\theta_2) \\ p \cos(\theta_2) e^{ik_{z2}d} + q \sin(\theta_2) e^{-ik_{z2}d} &= t \cos(\theta_3) e^{i(k_{z3}d - (n_2 - n_1)\phi_k / 2)} \\ p \sin(\theta_2) e^{ik_{z2}d} + q \cos(\theta_2) e^{-ik_{z2}d} &= t \sin(\theta_3) e^{i(k_{z3}d + (n_2 - n_1)\phi_k / 2)}\end{aligned}\quad (11)$$

Solving for r from these equations one obtains $r = \mathcal{N}/\mathcal{D}$

$$\begin{aligned}\mathcal{N} &= \cos(\theta_3) [\sin(\theta_1) + \sin(\theta_1 - 2\theta_2) + 2e^{2ik_{z2}d} \\ &\quad \times \sin(\theta_2) \cos(\theta_1 + \theta_2)] + \sin(\theta_3) e^{i(n_2 - n_1)\phi_k} [\cos(\theta_1) \\ &\quad - \cos(\theta_1 - 2\theta_2) - 2e^{2ik_{z2}d} \cos(\theta_2) \cos(\theta_1 + \theta_2)] \\ \mathcal{D} &= 2 [e^{i(n_2 - n_1)\phi_k} \sin(\theta_3) [e^{2idk_{z2}} \cos(\theta_2) \sin(\theta_1 - \theta_2) \\ &\quad + \sin(\theta_2) \cos(\theta_1 + \theta_2)] - \cos(\theta_3) [\cos(\theta_2) \cos(\theta_1 + \theta_2) \\ &\quad + e^{2idk_{z2}} \sin(\theta_2) \sin(\theta_1 - \theta_2)]]\end{aligned}\quad (12)$$

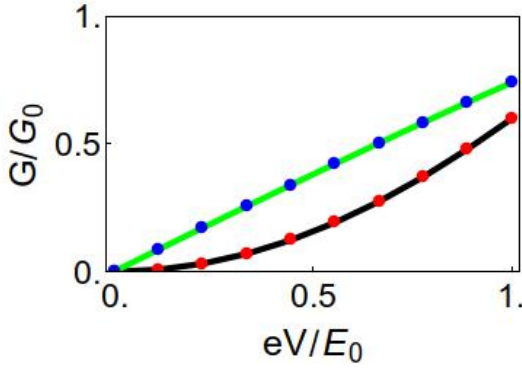


FIG. 2: (a) Plot of G/G_0 as a function of eV (in units of E_0) for $\delta n = \pm 1$. The black solid line (red dots) corresponds to $n_1 = 1$, $n_2 = 2$, and $\chi = 0(\pi/4)$ while the green solid line (blue dots) corresponds to $n_1 = 2$, $n_2 = 3$ and $\chi = 0(\pi/4)$. For all plots, $\epsilon_0 = \epsilon'_0 = \eta = 1$ and $\mu_N = 0$. See text for details.

The expression of the transmission and hence the conductance can be obtained using Eq. 12 as $T = 1 - |r|^2$ and

$$G = G_0 \int_0^{k_{\max}} \frac{k dk}{2\pi} \int_0^{2\pi} \frac{d\phi_k}{2\pi} T$$

$$G_0 = \frac{n_0 e^2}{h N_1}, \quad N_1 = \int_0^1 \frac{k dk}{2\pi} \int_0^{2\pi} \frac{d\phi_k}{2\pi} = \frac{1}{4\pi}. \quad (13)$$

Here $N_1 \equiv N_1 k_0^2$ denote the total number of transverse modes around a Weyl node up to the cutoff k_0 for which the continuum Weyl model used here holds, n_0 is the total number of Weyl nodes in the Brillouin zone each of which provides independent contribution to G , and $k_{\max} = \text{Min}[(eV + \mu_N)/\epsilon_0, [\eta(eV + \mu_N)/\epsilon'_0]^{1/n_2}]$ is the largest momentum channel participating in current transport across the junction. Note that k_{\max} is determined by the condition that both $\theta_1 = \arcsin[\epsilon_0 k^{n_1} / |eV + \mu_N|]/2$ and $\theta_3 = \arcsin[\epsilon'_0 k^{n_2} / (\eta|eV + \mu_N|)]/2$ must be real for a particular momentum channel to conduct.

Next, we note that in contrast to junctions between WSMs or two similar MSMs with $n_1 = n_2$, $|r|^2$, and hence T possess non-trivial ϕ_k dependence for the present junctions where $n_1 \neq n_2$. To understand this phenomenon better, we now move to the thin barrier limit. In this limit, it is easy to see that $\theta_2, k_{z3}d \rightarrow 0$, and $k_{z2}d \rightarrow -\chi$. The boundary conditions can then be written as

$$\psi_I(z = 0^-) = e^{i\tau_3 \chi} \psi_{III}(z = 0^+) \quad (14)$$

We note that this implies that the dimensionless barrier potential induces a rotation by -2χ in spin space about the z axis. For $n_1 = n_2$, this leads to oscillatory dependence of the conductance on χ . In contrast, for $n_1 \neq n_2$, since $\psi_{I[III]} \sim \exp[-i\tau_z n_1 [n_2] \phi_k / 2]$, the rotation induced by the barrier can be offset by changing $\phi_k \rightarrow \phi_k + \delta\phi$, where $\delta\phi = 2\chi/(n_2 - n_1)$. Thus the junction conductance, which involves a sum over all azimuthal angles,

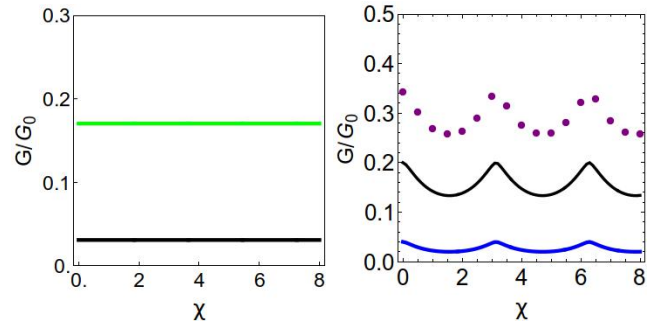


FIG. 3: (a) Plot of G/G_0 as a function of χ for $eV/E_0 = 0.2$. The black (green) solid lines correspond to $n_1 = 1(2)$ and $n_2 = 2(3)$. (b) Plot of G/G_0 as a function of χ for $n_1 = n_2 = n_0$ and $eV/E_0 = 0.2$. The blue solid, the black dashed, and the magenta dotted lines correspond to $n_0 = 1, 2$ and 3 respectively. All other parameters are same as in Fig. 2. See text for details.

is expected to become barrier independent in the thin barrier limit.

To verify this expectation, we first substitute $\theta_2, k_{z3}d \rightarrow 0$, and $k_{z2}d \rightarrow \chi$ in Eq. 12 and obtain, after a few lines of algebra,

$$T_{tb} = \frac{\mathcal{A}}{\mathcal{B} - \mathcal{C} \cos[(n_1 - n_2)\phi_k + 2\chi]}$$

$$\mathcal{A} = \cos(2\theta_1) \cos(2\theta_3), \quad \mathcal{C} = \sin(2\theta_1) \sin(2\theta_3)/2$$

$$\mathcal{B} = \sin^2(\theta_1) \sin^2(\theta_3) + \cos^2(\theta_1) \cos^2(\theta_3) \quad (15)$$

From Eq. 15, we find that in the presence of a change in winding number across region I and III ($n_1 \neq n_2$), χ appears as a phase shift to the azimuthal angle ϕ_k . Since \mathcal{A}, \mathcal{B} , and \mathcal{C} are independent of ϕ_k , the integration over ϕ_k in Eq. 13 is straightforward and yields

$$\int_0^{2\pi} \frac{d\phi_k}{2\pi} T_{tb} = T_1, \quad G = G_0 \int_0^{k_{\max}} \frac{k dk}{2\pi} T_1$$

$$T_1 = \frac{2 \cos(2\theta_1) \cos(2\theta_3)}{|\cos(2\theta_1) + \cos(2\theta_3)|} \quad (16)$$

We therefore find that G becomes independent of χ in the thin barrier limit according to our earlier expectation. This independence is a direct consequence of ϕ_k dependence of T which happens for $n_1 \neq n_2$. Thus such a barrier independence of G requires a change in the topological winding number across the junction; consequently, this effect would not show up in junctions between WSMs or MSMs with $n_1 = n_2$. We would like to point out that this phenomenon can only occur in $d > 2$ where there are more than one transverse directions; thus it does not have an analogue in 2D topological materials.

Next, we provide numerical support to our finding. To this end, we first obtain G/G_0 by numerically integrating T_{tb} over k and ϕ_k . For all numerical plots we shall choose $\eta = \epsilon'_0 = \epsilon_0 = 1$; we have checked that the numerical values of these quantities do not alter qualitative nature of the results presented. The corresponding results are

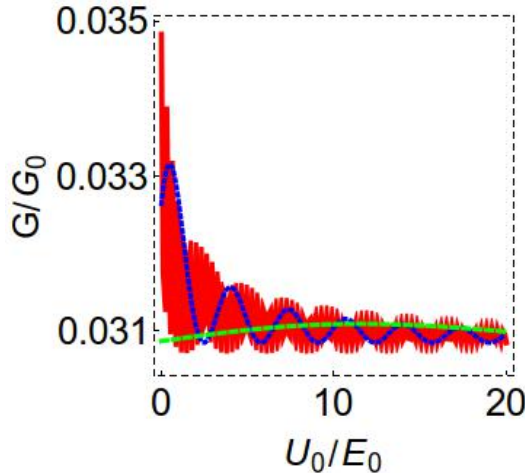


FIG. 4: Plot of G/G_0 as a function of U_0/E_0 for $dk_0 = 10$ (red solid line), 1 (blue dotted line) and 0.1 (green dashed line). For all plots $eV/E_0 = 0.2$, $n_1 = 1$, and $n_2 = 2$. All other parameters are same as in Fig. 2.

shown in Fig. 2 and 3. In Fig. 2, we show the variation of G/G_0 as a function of the applied voltage eV/E_0 in the thin barrier limit for $n_1 - n_2 = -1$ with $n_1 = 1$ and $n_1 = 2$ and for two representative values of $\chi = 0, \pi/4$. We have checked that the behavior of G is identical for $n_1 - n_2 = 1$ and qualitatively similar for $n_1 - n_2 = \pm 2$ for same n_1 . The different behavior of G as a function of eV/E_0 for $n_1 = 1$ and $n_1 = 2$ can be understood as follows. We note from Eq. 15 and 16 that for small eV , $\theta_3 \ll \theta_1$ (Eq. 9). Consequently one may approximate

$$T_1 \simeq \frac{2 \cos(2\theta_1)}{|1 + \cos(2\theta_1)|} = \frac{2\sqrt{1 - k^{2n_1}/(eV + \mu_0)^2}}{1 + \sqrt{1 - k^{2n_1}/(eV + \mu_0)^2}} \quad (17)$$

The integral T_1 over k can then be analytically performed and leads to $G/G_0 \sim k_{\max}^2 = c|eV + \mu_0|^{2/n_1}$, where c is a constant. Thus G/G_0 is a parabolic (linear) function of the applied voltage for $n_1 = 1(2)$ and $\mu_N = 0$. An exactly similar behavior emerges when $n_1 > n_2$ since T_1 is symmetric under the interchange of θ_3 and θ_1 . Note that for finite $\mu_N/E_0 < 1$ and $eV \ll \mu_N$, G/G_0 will always vary linearly with eV .

For both $n_1 = 1$ and $n_1 = 2$, from Fig. 2, we find that G/G_0 is independent of χ . This independence can be more directly seen from Fig. 3(a). We also note that such a barrier independence is absent if $n_1 = n_2$; this is easily seen from Fig. 3(b), where G oscillates with χ for a junction between two WSMs ($n_1 = n_2 = 1$) or MSMs ($n_1 = n_2 = 2, 3$). We note that these numerical results confirm our earlier analytical expectation that the χ independence of G is a consequence of the change in topological winding number across the junction.

Next, we investigate the fate of G as a function of U_0 away from the thin barrier limit for several representative values of d . To this end, we numerically compute $T = 1 - |r|^2$ from Eq. 12 and use Eq. 13 to obtain G . Fig.

4 shows a plot of G/G_0 as a function of U_0 for several representative values of d . We note that G/G_0 has small oscillatory dependence on U_0 ; the amplitude of these oscillations decay as U_0 is increased and G/G_0 becomes independent of U_0 for large U_0 . This is consistent with our earlier results in the thin barrier limit.

Before ending this section, we observe a few points regarding our analysis. First, we have carried out this analysis for ballistic junctions. The justification for such an analysis is two fold. First, it is well-known that Weyl semimetals, in the presence of weak disorder, hosts a quasi-ballistic regime²⁵. In this regime, we expect the computations carried out in the ballistic regime to be qualitatively correct as demonstrated earlier. For this one needs the typical mean-free path to be larger than the barrier region²⁶. Moreover we note that a scalar disorder potential in Weyl semimetals can not scatter between states with different $\phi_{\vec{k}}$. This can be seen through a direct calculation using Gaussian disorder potential^{25,26}; however, one can also understand this by noting that such a scattering would correspond to a spin rotation about \hat{z} which a scalar (spin-independent) disorder potential can not achieve. Thus the $\phi_{\vec{k}}$ dependence of the wavefunction which is central to the barrier independence discussed above is expected to be robust in the weak disorder regime. Second, we have neglected inter-node scattering. We note that as long as these Weyl nodes occur at different transverse momentum, the barrier can not lead to such inter-node scattering (since a barrier potential conserve transverse momenta on scattering). However, if the nodes occur at same transverse momentum such inter-node scattering can occur; we analyze this situation taking a simple model with two Weyl nodes at $\vec{k} = (0, 0 \pm K_0)$ in the Appendix. We show that long as $K_0 \gg d/a^2, eV/\hbar v_F, U_0/\hbar v_F$, such inter-node scattering is suppressed. Thus our analysis holds for a wide range of parameters which we chart out in the Appendix.

III. NBS JUNCTIONS

In this section, we study the transport through a NBS junction between a WSM and a MSM or two MSMs with different topological winding numbers. Throughout this section we shall work in the regime where the chemical potential μ_S in the superconduction region is large compared to the applied voltages but is small compared to E_0 . We note that the chemical potential μ_N shall be kept arbitrary. The schematic representation of such a junction is given by Fig. 5. The MSM (or WSM) in region III has a proximate s -wave superconductor. In this section, we shall consider, following Ref. 23, the case where the induced superconductivity is s -wave and the Cooper pairing connects two isotropic or anisotropic Weyl nodes with same chirality. The basis of this choice is the observation made in Ref. 23 that the inter-orbital superconduction pairing between nodes of opposite chirality is suppressed at low energy. We note that necessitates the

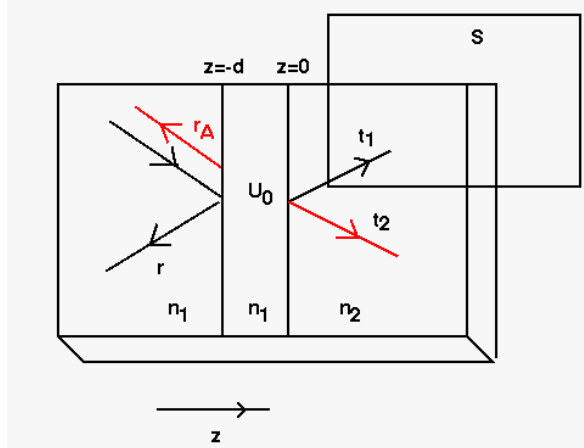


FIG. 5: A schemetaic representation of a NBS junction between two MSMs or a WSM and a MSM (characterized by topological winding numbers n_1 and n_2 as shown) in regions I and III separated by a barrier in region II ($-d \leq z \leq 0$). The barrier region II constitutes the same material as in region I but has an additional potential U_0 . Superconductivity is induced in region III via a proximate s -wave superconductor. The reflection, Andreev reflections and transmission amplitudes, r , r_A , t_1 and t_2 , for an electron approaching the barrier from region I, is shown schematically.

presence of at least four Weyl or multi-Weyl nodes in region III. With this model of induced superconductivity the Hamiltonian in region III is given by a 4×4 matrix

$$H_2^s = (H_2 - \mu_S) \otimes \sigma_3 + E_0 \eta^{-1} \Delta_0 I \otimes \sigma_1, \quad (18)$$

where σ_i for $i = 1, 2, 3$ denote Pauli matrices in particle-hole space, $\mu_S \gg eV$, Δ_0 is the chemical potential, and H_2 , given by Eq. 2, may represent a WSM or a MSM depending on the value of n_2 . Here we shall choose the phase of the superconducting condensate to be zero without any loss of generality. The basic excitations of H_2^s are Bogoliubov quasiparticles and quasiholes. The wavefunction of such right-moving quasiparticles, which would be necessary for our computation, are given by

$$\begin{aligned} \psi_{3e}^s &= e^{-i\tau_z n_2 \phi_k/2} (e^{i\mu_0} \cos \theta_3^s, e^{i\mu_0} \sin \theta_3^s, \cos \theta_3^s, \sin \theta_3^s)^T e^{i(k_x x + k_y y + k_{3z1}^s z)} / \sqrt{2} \\ \psi_{3h}^s &= e^{-i\tau_z n_2 \phi_k/2} (\cos \theta_3'^s, \sin \theta_3'^s, e^{i\mu_0} \cos \theta_3'^s, e^{i\mu_0} \sin \theta_3'^s)^T e^{i(k_x x + k_y y + k_{3z2}^s z)} / \sqrt{2} \end{aligned} \quad (19)$$

where $\tan(2\theta_3^s[\theta_3'^s]) = \epsilon_0' k^{n_2} / k_{3z1[2]}^s$. In Eq. 19, $k_{3z1[2]}^s$ correspond to electron-[hole]-like quasiparticles and are given by (for $\mu_S \gg eV, \Delta_0$)

$$\begin{aligned} k_{3z1[2]}^s &= +[-] \sqrt{(\mu_S \pm i\zeta)^2 \eta^2 - (\epsilon_0' k^{n_2})^2} \\ \zeta &= 1[i] \sqrt{\Delta_0^2 - (eV)^2}, \quad \text{for } eV \leq [\geq] \Delta_0 \\ \cos \mu_0 [\cosh \mu_0] &= eV/\Delta_0 \quad \text{for } eV \leq [\geq] \Delta_0. \end{aligned} \quad (20)$$

where we have scaled all energy scales by E_0 . We note

that the wavefunctions of the quasiparticles and quasiholes retain the property $\psi_{3e(h)}^s \sim \exp[-i\tau_z n_2 \phi_k/2]$.

The computation of tunneling conductance for such a junction follows the standard BTK formalism²⁷ applied to topological materials^{17,18,21}. To this end, we consider a right moving electron in region I approaching the barrier. Upon reflection (Andreev reflection) from the barrier, a left moving electron (hole) propagates to the left. The wavefunctions of these electron and holes are given by

$$\begin{aligned} \psi_{1eR} &= e^{i(k_x x + k_y y + k_{z1} z)} e^{-i\tau_z n_1 \phi_k/2} (\cos(\theta_1), \sin(\theta_1), 0, 0)^T \\ \psi_{1eL} &= e^{i(k_x x + k_y y - k_{z1} z)} e^{-i\tau_z n_1 \phi_k/2} (\sin(\theta_1), \cos(\theta_1), 0, 0)^T \\ \psi_{1hR} &= e^{i(k_x x + k_y y + k'_{z1} z)} e^{-i\tau_z n_1 \phi_k/2} (0, 0, -\sin(\theta'_1), \cos(\theta'_1))^T \\ \psi_{1hL} &= e^{i(k_x x + k_y y - k'_{z1} z)} e^{-i\tau_z n_1 \phi_k/2} (0, 0, \cos(\theta'_1), -\sin(\theta'_1))^T \end{aligned} \quad (21)$$

where $2\theta'_1 = \arcsin[\epsilon_0 k^{n_1} / |eV - \mu_N|]$ and $k'_{z1} = \text{Sgn}(eV - \mu_N + \epsilon_0 k^{n_1}) \sqrt{(eV - \mu_N)^2 - \epsilon_0^2 k^{2n_1}}$. In region I, the wave-

function can then be written as

$$\psi_I^{\text{nbs}} = \psi_{1eR} + r\psi_{1eL} + r_A\psi_{1hL} \quad (22)$$

where r and r_A denotes amplitude or ordinary and Andreev reflections respectively. We note that $\sin(\theta'_1) = -\sin(\theta_1)|(eV + \mu_N)|/|(eV - \mu_N)|$ so that $\theta'_1 \rightarrow -\theta_1$ for $\mu_N \gg eV$. Moreover, we find that $\psi_1 \sim e^{-i\tau_z n_1 \phi_k/2}$; thus for both electrons and holes, one can interpret ϕ_k dependence of the wavefunctions as a rotation in spin space about the z axis.

In region II, the wavefunctions of right/left moving electrons and holes are given by Eq. 21 with $k_{z1} \rightarrow k_{z2}$, $\theta_1 \rightarrow \theta_2$, $k'_{z1} \rightarrow k'_{z2}$, and $\theta'_1 \rightarrow \theta'_2$, where

$$\begin{aligned} 2\theta'_2 &= \arctan[\epsilon_0 k^{n_1} / k'_{z2}] \\ k'_{z2} &= \text{Sgn}(eV - \mu_N + U_0 + \epsilon_0 k^{n_1}) \\ &\times \sqrt{(eV - \mu_N + U_0)^2 - \epsilon_0^2 k^{2n_1}}. \end{aligned} \quad (23)$$

We note that θ'_2 is related to θ'_1 by the relation $2\theta'_2 = \arcsin[\sin(2\theta'_1)/|1 - U_0/(eV - \mu_N)|]$. The wavefunction in region II is thus given by

$$\psi_{II}^{\text{nbs}} = p_1\psi_{2eR} + p_2\psi_{2LR} + p_3\psi_{2hL} + p_4\psi_{2hR} \quad (24)$$

In region III, the wavefunctions constitutes a superposition of electron-like and hole-like quasiparticles are given by

$$\psi_{III}^{\text{nbs}} = t_1\psi_{3e}^s + t_2\psi_{3h}^s \quad (25)$$

where $\psi_{3e(h)}^s$ are wavefunctions of electron- and hole-like quasiparticles given by Eq. 19. We note that one can express θ_3^s and θ'_3^s in terms of θ_1 and θ'_1 as

$$\begin{aligned} \sin(2\theta_3^s) &= \frac{\epsilon'_0 [\sin(2\theta_1)|eV + \mu_N|]^{n_2/n_1}}{\epsilon_0^{n_2/n_1} \eta(\mu_S + i\zeta)} \\ \sin(2\theta'_3^s) &= -\frac{\epsilon'_0 \sin(2\theta'_1)|eV - \mu_N|}{\epsilon_0^{n_2/n_1} \eta(\mu_S - i\zeta)} \end{aligned} \quad (26)$$

Also, we find that $\psi_3^{\text{nbs}} \sim e^{-i\tau_z n_1 \phi_k/2}$.

To compute r and r_A , we need to match the boundary conditions on the wavefunctions at $x = -d$ and $x = 0$ (Fig.5): $\psi_I^{\text{nbs}}(z = -d) = \psi_{II}^{\text{nbs}}(z = -d)$ and $\psi_{III}^{\text{nbs}}(z = 0) = \psi_{II}^{\text{nbs}}(z = 0)$. The boundary condition at $z = -d$ leads to

$$\begin{aligned} \cos(\theta_1)e^{-ik_{z1}d} + r\sin(\theta_1)e^{ik_{z1}d} &= p_1\cos(\theta_2)e^{-ik_{z2}d} + p_2\sin(\theta_2)e^{ik_{z2}d} \\ \sin(\theta_1)e^{-ik_{z1}d} + r\cos(\theta_1)e^{ik_{z1}d} &= p_1\sin(\theta_2)e^{-ik_{z2}d} + p_2\cos(\theta_2)e^{ik_{z2}d} \\ r_A\cos(\theta'_1)e^{ik'_{z1}d} &= p_4\cos(\theta'_2)e^{ik'_{z2}d} - p_3\sin(\theta'_2)e^{-ik'_{z2}d} \\ r_A\sin(\theta'_1)e^{ik'_{z1}d} &= p_4\sin(\theta'_2)e^{ik'_{z2}d} - p_3\cos(\theta'_2)e^{-ik'_{z2}d} \end{aligned} \quad (27)$$

while that at $z = 0$ yields

$$\begin{aligned} \left[t_1\cos(\theta_3^s)e^{i\mu_0} + t_2\cos(\theta'_3^s) \right] e^{i(n_1-n_2)\phi_k/2}/\sqrt{2} &= p_1\cos(\theta_2) + p_2\sin(\theta_2) \\ \left[t_1\sin(\theta_3^s)e^{i\mu_0} + t_2\sin(\theta'_3^s) \right] e^{-i(n_1-n_2)\phi_k/2}/\sqrt{2} &= p_1\sin(\theta_2) + p_2\cos(\theta_2) \\ \left[t_1\cos(\theta_3^s) + t_2\cos(\theta'_3^s)e^{i\mu_0} \right] e^{i(n_1-n_2)\phi_k/2}/\sqrt{2} &= p_4\cos(\theta'_2) - p_3\sin(\theta'_2) \\ \left[t_1\sin(\theta_3^s) + t_2\sin(\theta'_3^s)e^{i\mu_0} \right] e^{-i(n_1-n_2)\phi_k/2}/\sqrt{2} &= -p_4\sin(\theta'_2) + p_3\cos(\theta'_2) \end{aligned} \quad (28)$$

To compute the conductance, we solve for r and r_A numerically using Eqs. 27 and 28. One can then obtain $T_s = (1 - |r|^2 + |r_A|^2)$ and obtain the tunneling conductance of the junction using²¹

$$G_s = G_{0s} \int_0^{k_{\text{max}}^s} \frac{k dk}{2\pi} \int_0^{2\pi} \frac{d\phi_k}{2\pi} T_s \quad (29)$$

where $k_{\text{max}}^s = \text{Min}[(|eV + \mu_N|/\epsilon_0)^{1/n_1}, (|eV - \mu_N|/\epsilon_0)^{1/n_1}]$ and $G_{0s} = (eV + \mu_N)^{2/n_1} e^2 / (4\pi\hbar)$ is the normal state

conductance of region I. Note that the expression of k_{max}^s follows from the requirement that both $\sin(\theta_1)$ and $\sin(\theta'_1)$ be real. We shall use Eq. 29 along with Eq. 26 for all numerical computations presented in this section.

To make further analytical process, we now resort to the thin-barrier limit, for which $U_0 \rightarrow \infty$ and $d \rightarrow 0$ with $\chi = U_0 d / \hbar v_F$ held fixed. As in Sec. II, in this limit $\theta_2, \theta'_2, k_{z1}d, k'_{z1}d \rightarrow 0$ and $k_{z2}d, [k'_{z2}d] \rightarrow -[+] \chi$. Consequently, it is easy to eliminate p_1, p_2, p_3 and p_4 from

Eqs. 27 and 28. The boundary condition in the thin barrier limit can again be written as $\psi_I^{\text{nbs}}(z = 0^-) = \exp[i\tau_3\chi]\psi_{III}^{\text{nbs}}(z = 0^+)$. Thus we once again expect barrier independence of G following the same logic charted out in Sec. II.

To verify this expectation, we first write out the above-mentioned boundary condition equations explicitly. This leads to a set of four equations for r , r_A , t_1 and t_2 given by

$$\begin{aligned} t_1 \cos(\theta_3^s) e^{i\mu_0} + t_2 \cos(\theta_3'^s) &= \sqrt{2} e^{-i\alpha_0} (\cos(\theta_1) + r \sin(\theta_1)) \\ t_1 \sin(\theta_3^s) e^{i\mu_0} + t_2 \sin(\theta_3'^s) &= \sqrt{2} e^{i\alpha_0} (\sin(\theta_1) + r \cos(\theta_1)) \\ t_1 \cos(\theta_3^s) + t_2 \cos(\theta_3'^s) e^{i\mu_0} &= \sqrt{2} r_A \cos(\theta_1') e^{-i\alpha_0} \\ t_1 \sin(\theta_3^s) + t_2 \sin(\theta_3'^s) e^{i\mu_0} &= \sqrt{2} r_A \sin(\theta_1') e^{i\alpha_0} \end{aligned} \quad (30)$$

$$\begin{aligned} \mathcal{Y} &= e^{2i\mu_0} \left[(e^{2i\alpha_0} \cos(\theta_3^s) \sin(\theta_1) - \cos(\theta_1) \sin(\theta_3^s)) \sin(\theta_1' - \theta_3'^s) + (e^{2i\alpha_0} \cos(\theta_3'^s) \sin(\theta_1) - \cos(\theta_1) \sin(\theta_3'^s)) \sin(\theta_1' - \theta_3^s) \right] \\ \mathcal{Z} &= \sin(\theta_1) \left[\sin(\theta_3^s) \left(e^{2i\mu_0} \sin(\theta_1' - \theta_3'^s) + \cos(\theta_1') \sin(\theta_3'^s) \right) - \sin(\theta_1') \cos(\theta_3^s) \sin(\theta_3'^s) \right] \\ &\quad - e^{2i\alpha_0} \cos(\theta_1) \left[\cos(\theta_3^s) \left(e^{2i\mu_0} \sin(\theta_1' - \theta_3'^s) + \sin(\theta_1') \cos(\theta_3'^s) \right) + \sin(\theta_3^s) \cos(\theta_1') \cos(\theta_3'^s) \right] \end{aligned} \quad (31)$$

We note that both R and R_A displays a non-trivial ϕ_k dependence if $n_2 \neq n_1$. Further, in the thin barrier limit, the dimensionless barrier strength χ always appear as a

where $\alpha_0 = (n_1 - n_2)\phi_k/2 + \chi$. Solving for r and r_A one obtains, in the thin barrier limit, we obtain $R^{\text{tb}} = |r|^2 = |\mathcal{Y}/\mathcal{Z}|^2$ and $R_A^{\text{tb}} = |r_A|^2 = \cos^2(2\theta_1)|\sin(\theta_3^s - \theta_3'^s)/\mathcal{Z}|^2$, where \mathcal{Y} and \mathcal{Z} are given by

$$T_s^{\text{tb}} = (1 - R^{\text{tb}} + R_A^{\text{tb}}) = \frac{N_s^{\text{tb}}}{D_s^{\text{tb}}} = \frac{N_1 + N_2 \cos[(n_1 - n_2)\phi_k + 2\chi + \beta_0] + N_3 \cos[2(n_1 - n_2)\phi_k + 4\chi]}{1 + D_1 \cos[(n_1 - n_2)\phi_k + 2\chi + \beta'_0] + D_2 \cos[2(n_1 - n_2)\phi_k + 4\chi]} \quad (32)$$

where $N_{1,2,3}$, β_0 , β'_0 , and $D_{1,2}$ are complicated functions of θ_3^s , $\theta_3'^s$, θ_1 and θ_1' . They are independent of χ and ϕ_k ; consequently their precise forms will not be relevant for the subsequent discussion. In fact, from Eq. 32, it is easy to check that $\int_0^{2\pi} d\phi_k T_s^{\text{tb}}$ is independent of χ irrespective of the functional forms of $N_{1,2,3}$, β_0 , β'_0 and $D_{1,2}$. The simplest way to see this is to use the standard substitution $z = \exp[i\{(n_1 - n_2)\phi_k + 2\chi\}]$ and convert the integral over ϕ_k to a complex integral over unit circle. The denominator, written in terms of z , is a quartic polynomial in z leading to four poles inside the unit circle. The residues of these poles do not depend on χ . Thus we expect that G_s will be independent of χ in the thin barrier limit. We once again note that as in NBN junctions, the χ independence is a consequence of change in the topological winding number across the junction; G_s will be an oscillatory function of χ if $n_1 = n_2$.

The qualitative reasoning presented above can be supported by numerics in the thin barrier limit presented

phase shift to $(n_1 - n_2)\phi_k$. One can now aim to compute the transmission T_s^{tb} and perform the ϕ_k integral. To this end, we find, after a cumbersome calculation,

Figs. 6 and 7. From Fig. 6, we find that the subgap tunneling conductance vanishes for $n_2 > n_1$ but remains finite for $n_2 \leq n_1$. Moreover G_s is independent of χ . This barrier independence is further highlighted in Fig. 7, where we find that the zero-bias conductance ($G_s(eV = 0)$) becomes independent of χ in the thin barrier limit for $n_1 \neq n_2$; in contrast for $n_1 = n_2$, a clear oscillatory behavior is found.

The suppression of G_s for $eV \leq \Delta_0$ and $n_2 > n_1$ in Figs. 6(a) and 6(b) can be qualitatively understood from Eq. 26. We first note that our numerical results for the thin barrier limit are presented for $\mu_s = \mu_N \gg eV, \Delta_0$ and $\epsilon_0 = \epsilon'_0 = \eta = 1$. In this limit, one finds, from Eq. 26, $\sin(2\theta_3^s) \simeq (\sin(2\theta_1))^{n_2/n_1} \mu_N^{n_2/n_1 - 1}$. Thus for $eV \leq \Delta_0$, θ_3^s has no real solution for a majority of the transverse channels for which $(\sin(2\theta_1))^{n_2/n_1} > \mu_N^{1-n_2/n_1}$. For these transverse modes, $\sin(2\theta_3^s), \cos(2\theta_3^s) \rightarrow i \exp[(\sin(2\theta_1))^{n_2/n_1} \mu_N^{n_2/n_1 - 1}] / 2$ for

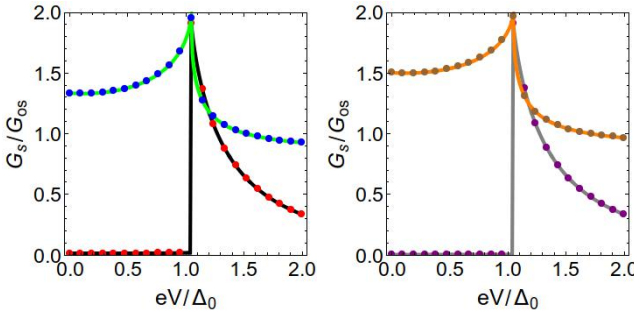


FIG. 6: (a) Plot of G_s/G_{0s} as a function of eV/Δ_0 for $\delta n = \pm 1$. The black solid line (red dots) corresponds to $n_2 = 2$, $n_1 = 1$, and $\chi = 0(\pi/4)$ while the blue solid line (green dots) corresponds to $n_2 = 1$, $n_1 = 2$ and $\chi = 0(\pi/4)$. (b) Plot of G_s/G_{0s} as a function of eV/Δ_0 for $\delta n = \pm 2$. The grey solid line (pink dots) corresponds to $n_2 = 3$ and $n_1 = 1$ and $\chi = 0(\pi/4)$ while the orange solid line (brown dots) corresponds to $n_2 = 1$, $n_1 = 3$ and $\chi = 0(\pi/4)$. For all plots, $\epsilon_0 = \epsilon'_0 = \eta = 1$ and $\mu_N = \mu_S = 100\Delta_0$. See text for details.

large μ_N . A similar behavior is found for $\theta_3'^s$. Thus from Eq. 31 one finds that for these modes $\mathcal{Z} \sim \exp[(\sin(\theta_1))^{n_2/n_1} \mu_N^{n_2/n_1-1}]$. Thus $R_A \sim \sin^2(\theta_3^s - \theta_3'^s)/|\mathcal{Z}|^2 \sim \exp[-\mu_N^{n_2/n_1-1}(\sin(2\theta_1))^{n_2/n_1}]$ and vanishes exponentially for these modes. It is also easy to see that $R \rightarrow 1$ for these modes. The number of such modes constitute a majority of the total available transverse modes for large μ_N ; consequently, $G_s(eV \leq \Delta_0) \rightarrow 0$ in this limit. We note that the suppression of the subgap tunneling conductance for large μ_N and μ_S is completely controlled by the change of the topological winding numbers n_1 and n_2 across the junctions. In contrast, for $n_2 < n_1$, $\theta_3^s \rightarrow 0$, since $\mu_N^{n_2/n_1-1} \ll 1$ in this regime. Similarly, from Eq. 26, we find that $\theta_3'^s \rightarrow \pi/2$ in this limit. Thus R_A remain finite and one finds finite subgap G_s as can be seen in Fig. 6. Thus we conclude that the subgap tunneling conductance of these junctions depends crucially on the ratio n_2/n_1 . We note that for $n_1 = 1, n_2 = 1$, our results reproduces those in Ref. 23 for $\mu_N, \mu_S \gg \Delta_0$ as special case.

Finally, we consider deviation from the thin barrier limit. To this end, we numerically evaluate the conductance using Eqs. 27, 28, and 29 and plot the zero-bias conductance $G_s(eV = 0)/G_{0s}$ as a function of U_0/Δ_0 for several representative values of d in Fig. 8. As in the case of NBN junctions, we find that $G_s(eV = 0)/G_{0s}$ shows oscillatory behavior for large d ; however the amplitude of these oscillations decay with increasing U_0 and approaches the thin barrier behavior for either large U_0/Δ_0 or small d . We note that even for large d , a sufficiently large value of U_0/Δ_0 can lead to near constant behavior of G_s which is expected to make this behavior experimentally easy to verify.

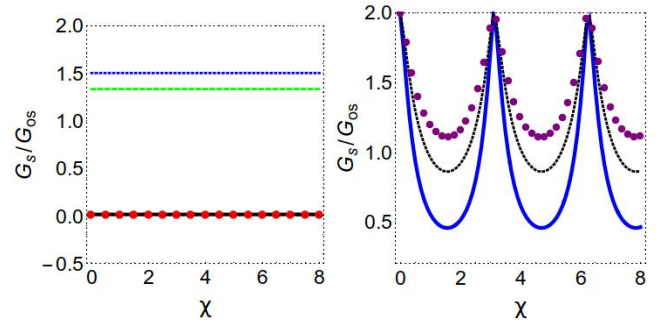


FIG. 7: (a) Plot of zero-bias conductance $G_s(eV = 0)/G_{0s}$ as a function of χ . The black solid line (red dots) correspond to $n_1 = 1$ and $n_2 = 2(3)$ while the blue solid (green dashed) lines correspond to $n_2 = 1$ and $n_1 = 2(3)$. (b) Plot of $G(eV = 0)/G_{0s}$ as a function of χ for $n_1 = n_2 = n_0$. The blue solid, the black dashed, and the magenta dotted lines correspond to $n_0 = 1, 2$ and 3 respectively. All other parameters are same as in Fig. 6. See text for details.

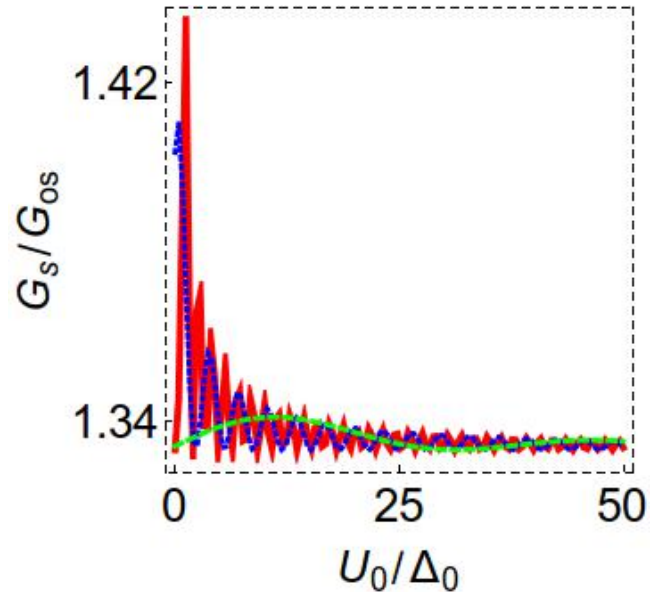


FIG. 8: (a) Plot of zero-bias conductance $G_s(eV = 0)/G_{0s}$ as a function of U_0/Δ_0 for $n_1 = 2$, $n_2 = 1$, and $\mu_N = 0.1\Delta_0$ and $\mu_S = 100\Delta_0$. The red solid line correspond to $dk_0 = 10$, the blue dotted line to $dk_0 = 1$, and the green dashed line to $dk_0 = 0.1$. See text for details.

IV. DISCUSSION

In this work, we have studied the tunneling conductance between junctions of a WSM and a MSM (or two MSMs) where the topological winding numbers of the Weyl nodes change across the junction. We have shown that the tunneling conductance of such junctions exhibits several unconventional features which are absent both in junctions involving 2D topological materials such graphene or topological insulators surfaces and in those made out of 3D topological materials such as WSMs or

MSMs with $n_1 = n_2$. The most striking of such features is the barrier independence of G and G_s in the thin barrier limit. We note that such a feature is in sharp contrast to both Schrodinger materials (where G decays monotonically with increasing χ) and previously studied topological materials (where G oscillates with χ). We demonstrate that such barrier independence is a consequence of the change in topological winding number of the Weyl nodes across the junction. Moreover, for NBS junctions with $\mu_S, \mu_N \gg eV, \Delta_0$, the subgap tunneling conductance $G_s(eV \leq \Delta_0)$ vanishes when $n_2 > n_1$; however, it is finite when $n_1 > n_2$. Thus the subgap tunneling conductance of such NBS junctions depend crucially on the ratio of the topological winding numbers of the WSMs/MSMs forming the junction.

The simplest experimental verification of our work would require formation of a junction between a WSM and MSM. The longitudinal direction of such junctions needs to be the symmetry axis of the MSM (taken to be \hat{z} in our work). The barrier regions can be simulated by putting an additional local gate voltage U_0 on the WSM in a region of width d . For large U_0 , we predict that $G(eV)$ will be independent of the dimensionless barrier strength χ . Another, experimentally more challenging, possibility would be to study the subgap tunneling conductance of such junctions when superconductivity is induced either on the WSM or the MSM. We predict that the subgap tunneling conductance $G_s(eV \leq \Delta_0)$ in these two cases will show qualitatively different behavior for $\mu_S, \mu_N \gg eV, \Delta_0$. For the case, when superconductivity is induced in the MSM, G_s will vanish; in contrast it will be finite, if superconductivity is induced in the WSM. However, in both cases, G_s will be independent of χ for large U_0 . We note that such features can also be observed in a junction constructed out of two MSMs of similar material provided one applies a sufficiently large strain on one of them¹⁰. This would split the Weyl nodes leading to $n = 1$ in that region while the other region of the junction will still have $n \neq 1$. This will lead to the crucial jump in topological winding number across the junction and lead to predicted the barrier independent transport.

In conclusion, we have studied transport in NBN and NBS junctions between a WSM and a MSM or two MSMs with different topological winding numbers. We have demonstrated barrier independence of tunneling conductance for such junctions in the thin barrier limit and analyzed the role of the topological winding numbers in shaping the applied voltage dependence of their tunneling conductance. We have discussed experimental signatures of these phenomena.

Acknowledgement: KS thanks Pushan Majumdar, Koushik Ray, and Diptiman Sen for several discussions.

Appendix A: Inter-node scattering

In this appendix, we discuss the effect of inter-node scattering on the conductivity calculations for NBN junctions. First, we note that since the potential barrier conserves transverse momentum on scattering such inter-node scattering can only occur if the Weyl nodes occur at same transverse momentum. To this end, we consider a model Hamiltonian with two Weyl nodes at $(0, 0, \pm K_0)$ which is given by

$$H_w = E_0 \sum_{\vec{k}} \psi_{\vec{k}}^{\dagger} ((k_z^2 - K_0^2) \tau_z + \alpha_{n_1} k^{n_1} [\cos(n_1 \phi_{\vec{k}}) \tau_x + \tau_y \sin(n_1 \phi_{\vec{k}})]) \psi_{\vec{k}} \quad (A1)$$

where $E_0 = \hbar^2/(2ma^2)$ is the unit of energy, a is the lattice spacing, all $k_{x,y,z}$ are measured in units of a^{-1} , $\phi_{\vec{k}} = \arctan[k_y/k_x]$, α_{n_1} is a material specific constant, $k = \sqrt{k_x^2 + k_y^2}$ is the magnitude of the transverse momentum, and n_1 is the topological winding number of the nodes. In what follows we are going to study transport through an NBN junction whose basic quasiparticle excitations are governed by H_w allowing for inter-node scattering between the two Weyl nodes²⁴. The schematic picture of such a junction is shown in Fig. 1 of the main text. The analysis carried out here will be similar to that in the main text and we are going to present the salient features which are different due to the presence of inter-node scattering. We note that the energy dispersion of H_w is given by

$$E_w = \pm \sqrt{(k_z^2 - K_0^2)^2 + \alpha_{n_1}^2 |k|^{2n_1}} \quad (A2)$$

The wavefunction in region I is now a superposition of that of an incident electron at the node $(0, 0, K_0)$ (which we shall denote as node 1) with momentum k_z^+ and two reflected electrons at the two nodes with momenta k_z^- (intra-node) and $-k_z^+$ (inter-node). The expressions for these momenta and the corresponding electron wavefunctions can be easily found using Eqs. A1 and A2 and is given by

$$\begin{aligned} k_z^{\pm} &= \sqrt{K_0^2 \pm \sqrt{(eV + \mu_N)^2 - \alpha_{n_1}^2 k^{2n_1}}} \\ \psi_{\text{in}1} &= e^{i(k_z^+ z + k_x x + k_y y - n_1 \sigma_z \phi_{\vec{k}}/2)} \frac{1}{\sqrt{1 + \eta_1^2}} \begin{pmatrix} 1 \\ \eta_1 \end{pmatrix} \\ \psi_{\text{ref}1} &= e^{i(k_z^- z + k_x x + k_y y - n_1 \sigma_z \phi_{\vec{k}}/2)} \frac{1}{\sqrt{1 + \eta_1^2}} \begin{pmatrix} \eta_1 \\ 1 \end{pmatrix} \\ \psi'_{\text{ref}2} &= e^{i(-k_z^+ z + k_x x + k_y y - n_1 \sigma_z \phi_{\vec{k}}/2)} \frac{1}{\sqrt{1 + \eta_1^2}} \begin{pmatrix} 1 \\ \eta_1 \end{pmatrix} \end{aligned} \quad (A3)$$

Here $\psi_{\text{ref}1}$ ($\psi_{\text{ref}2}$) are the wavefunctions of the electrons reflected at the same (opposite) node, $\eta_1 = \arcsin[\alpha_{n_1} k^{n_1} / (eV + \mu_N)]$, and we have chosen the energy of the incident electron to be $\epsilon = eV + \mu_N$. Thus the wavefunction in region I is given by

$$\psi_I = \psi_{\text{in}1} + r_1 \psi_{\text{ref}1} + r_2 \psi_{\text{ref}2} \quad (A4)$$

where r_1 and r_2 are the amplitudes of intra- and inter-node reflection respectively.

In region II, the wavefunction is a linear superposition of left and right moving electrons in both nodes. The wavefunctions for the right moving electrons in the node situated in $(0, 0, K_0)$ and the left moving electrons in both nodes can be read off from Eq. A3. Indeed their expressions are given by Eq. A3 with $k_z^\pm \rightarrow k_z'^\pm = \sqrt{K_0^2 \pm \sqrt{(eV + \mu_N - U_0)^2 - \alpha_{n_1}^2 k^{2n_1}}}$ and $\eta_1 \rightarrow \eta_2 = \arcsin[\alpha_{n_1} k^{n_1} / (eV + \mu_N - U_0)]$. We denote these wavefunctions by $\psi'_{\text{in}1}$, $\psi'_{\text{ref}1}$ and $\psi'_{\text{ref}2}$. The wavefunction for the right moving electron around the second Weyl node $(0, 0, -K_0)$ (which we shall denote as node 2) is given by

$$\psi'_{\text{in}2} = e^{i(-k_z'^- z + k_x x + k_y y - n_1 \sigma_z \phi_{\vec{k}}/2)} \frac{1}{\sqrt{1 + \eta_2^2}} \begin{pmatrix} \eta_2 \\ 1 \end{pmatrix} \quad (\text{A5})$$

The wavefunction in region II can be written in terms of these wavefunctions as

$$\psi_{II} = p_1 \psi'_{\text{in}1} + p_2 \psi'_{\text{in}2} + q_1 \psi'_{\text{ref}1} + q_2 \psi'_{\text{ref}2} \quad (\text{A6})$$

where $p_{1,2}(q_{1,2})$ are the amplitudes of right (left) moving electrons in nodes 1 or 2.

In region III, the wavefunction is a linear combination of right-moving electron wavefunctions on both nodes. These are obtained from Eq. A3 and A5 with the substitution of $\mu_N \rightarrow \mu'_N$, $n_1 \rightarrow n_2$, $k_z^\pm \rightarrow k_{3z}^\pm = \sqrt{K_0^2 \pm \sqrt{(eV + \mu'_N)^2 - \alpha_{n_2}^2 k^{2n_2}}}$ and $\eta_1 \rightarrow \eta_3 = \arcsin[\alpha_{n_2} k^{n_2} / (eV + \mu'_N)]$. We denote these wavefunctions by ψ_3 and ψ'_3 . The wavefunction in this region are given by

$$\psi_{III} = t \psi_3 + t' \psi'_3 \quad (\text{A7})$$

where t and t' denote amplitudes of transmission of electrons in node 1 and node 2 respectively.

The current conservation at the boundaries, *i.e.*, at $z = 0$ and $z = d$, requires the continuity of the wavefunction and their z derivatives at $z = 0$ and $z = d$. The conditions $\psi_I(z = 0) = \psi_{II}(z = 0)$ and $\partial_z \psi_I(z = 0) = \partial_z \psi_{II}(z = 0)$ yields

$$\begin{aligned} \frac{1}{\sqrt{1 + \eta_1^2}}(1 + r_1 + \eta_1 r_2) &= \frac{1}{\sqrt{1 + \eta_2^2}}(p_1 + q_1 + \eta_2(p_2 + q_2)) \\ \frac{1}{\sqrt{1 + \eta_1^2}}(\eta_1(1 + r_1) + r_2) &= \frac{1}{\sqrt{1 + \eta_2^2}}(\eta_2(p_1 + q_1) + p_2 + q_2) \\ \frac{1}{\sqrt{1 + \eta_1^2}}(k_z^+(1 - r_1) + \eta_1 k_z^- r_2) &= \frac{1}{\sqrt{1 + \eta_2^2}}((p_1 - q_1)k_z'^+ - \eta_2 k_z'^-(p_2 - q_2)) \\ \frac{1}{\sqrt{1 + \eta_1^2}}(\eta_1 k_z^+(1 - r_1) + k_z^- r_2) &= \frac{1}{\sqrt{1 + \eta_2^2}}((p_1 - q_1)\eta_2 k_z'^+ - k_z'^-(p_2 - q_2)) \end{aligned} \quad (\text{A8})$$

Similarly the conditions $\psi_{II}(z = d) = \psi_{III}(z = d)$ and $\partial_z \psi_{II}(z = d) = \partial_z \psi_{III}(z = d)$ yields

$$\begin{aligned} \frac{1}{\sqrt{1 + \eta_3^2}}[t e^{i k_z^+ d} + \eta_3 t' e^{i k_z^- d}] &= \frac{1}{\sqrt{1 + \eta_2^2}}(p_1 e^{i k_z'^+ d} + q_1 e^{-i k_z'^+ d} + \eta_2(p_2 e^{-i k_z'^- d} + q_2 e^{i k_z'^+ d})) e^{-i \nu'} \\ \frac{1}{\sqrt{1 + \eta_3^2}}[t \eta_3 e^{i k_z^+ d} + t' e^{i k_z^- d}] &= \frac{1}{\sqrt{1 + \eta_2^2}}(\eta_2(p_1 e^{i k_z'^+ d} + q_1 e^{-i k_z'^+ d}) + p_2 e^{-i k_z'^- d} + q_2 e^{i k_z'^+ d}) e^{i \nu'} \\ \frac{1}{\sqrt{1 + \eta_3^2}}[t k_z^+ e^{i k_z^+ d} + \eta_3 k_z^- t' e^{i k_z^- d}] &= \frac{1}{\sqrt{1 + \eta_2^2}}(k_z'^+(p_1 e^{i k_z'^+ d} - q_1 e^{-i k_z'^+ d}) - k_z'^-(\eta_2(p_2 e^{-i k_z'^- d} - q_2 e^{i k_z'^+ d})) e^{-i \nu'} \\ \frac{1}{\sqrt{1 + \eta_3^2}}[t \eta_3 k_z^+ e^{i k_z^+ d} + k_z^- t' e^{i k_z^- d}] &= \frac{1}{\sqrt{1 + \eta_2^2}}(\eta_2 k_z'^+(p_1 e^{i k_z'^+ d} - q_1 e^{-i k_z'^+ d}) - k_z'^-(p_2 e^{-i k_z'^- d} - q_2 e^{i k_z'^+ d})) e^{i \nu'} \end{aligned} \quad (\text{A9})$$

where $\nu' = (n_2 - n_1)\phi_k/2$. In what follows, we shall numerically solve Eq. A8 and A9 to obtain r_1 and r_2 .

The conductance can then be computed as

$$\begin{aligned} G(eV) &= 2G_0 \int d^2 k_y T(k_x, k_y; eV), \\ T(k_x, k_y; eV) &= (1 - |r_1|^2 v_{z2}/v_{z1} - |r_2|^2) \end{aligned} \quad (\text{A10})$$

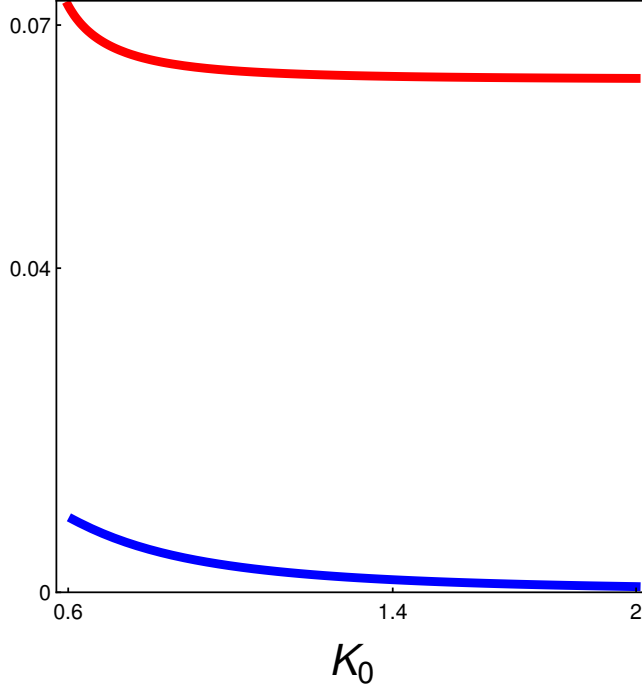


FIG. 9: Plot of inter-node scattering probability $R_{1,2} = \int d^2k |r_{1,2}|^2$ as a function of K_0 (all momenta are in units of a). The blue solid line represents the inter-node scattering probability R_1 and the red line R_2 . Here $eV = 0.01$, $\mu_L = 0.1$, $\mu_R = 0.3$, $U_0 = 0.5$, $n_1 = n_2 = 1$, and $d = 0.2$. All energy scales are in units of $\hbar^2/(2ma^2)eV = 0.01$.

where G_0 is defined in the main text with $n_0 = 2$ and $v_{z1,2}$ are the longitudinal velocities of the Weyl fermions in the two nodes. Comparing Eq. A10 with Eq. 13 of the main text, we find that they coincide when $|r_1|^2 \rightarrow 0$. This is also the regime where the approximation used in the main text should work.

The behavior of the $R_{1,2} = \int d^2k |r_{1,2}|^2$ is shown in Fig. 9 for a representative value of μ_R , d , eV , U_0 and μ_L . We note that for large enough K_0 , the inter-valley scattering is largely suppressed and one finds that for $K_0a \geq 0.5$, the inter-node scattering can be safely neglected compared to the intra-node scattering. This behavior is seen for all parameter values that we have checked. Thus we note that as long as the Weyl nodes are far off in momentum space, for low-energy transport, it is possible to work within independent node approximation as done in the main text. Indeed as seen from the behavior of G/G_0 in Fig. 10, G/G_0 becomes almost independent of K_0 in this limit. Thus we expect that for large enough $K_0a > 0.5$, inter-node scattering do not affect conductance. Indeed, comparing G/G_0 in Fig. 2, to G/G_0 computed by setting $T = 1 - |r_2|^2$ (i.e. by setting $r_1 = 0$) yields a near-perfect match.

Next, we consider the thin barrier limit in these junctions. This limit is given by $E_0 K_0^2 a^2 \gg U_0 \gg \mu_N + eV$. In this limit one finds $\chi = U_0 d / (2\hbar v_F K_0) \ll K_0 d$, $k_{z2}^{\pm} d = K_0 d \pm \chi$, $\eta_2 \rightarrow 0$, and $k_{3z} d, k'_{3z} d \rightarrow 0$. In this limit, it is easy to see that Eqs. A8 and A9 reduces to

$$\begin{aligned}
\frac{1}{\sqrt{1 + \eta_1^2}}(1 + r_1 + \eta_1 r_2) &= p_1 + q_1 \\
\frac{1}{\sqrt{1 + \eta_1^2}}(\eta_1(1 + r_1) + r_2) &= p_2 + q_2 \\
\frac{1}{\sqrt{1 + \eta_1^2}}(k_z^+(1 - r_1) + \eta_1 k_z^- r_2) &= (p_1 - q_1)K_0 \\
\frac{1}{\sqrt{1 + \eta_1^2}}(\eta_1 k_z^+(1 - r_1) + k_z^- r_2) &= K_0(p_2 - q_2) \\
\frac{1}{\sqrt{1 + \eta_3^2}}(t + \eta_3 t') &= [p_1 e^{iK_0 d} + q_1 e^{-iK_0 d}]e^{-i\nu} \\
\frac{1}{\sqrt{1 + \eta_3^2}}[t\eta_3 + t'] &= (p_2 e^{-iK_0 d} + q_2 e^{iK_0' d})e^{i\nu} \\
\frac{1}{\sqrt{1 + \eta_3^2}}[t k_z^+ + \eta_3 k_z^- t'] &= (K_0(p_1 e^{iK_0 d} - q_1 e^{-iK_0 d}))e^{-i\nu} \\
\frac{1}{\sqrt{1 + \eta_3^2}}[t k_z^+ \eta_3 + k_z^- t'] &= \frac{-1}{\sqrt{1 + \eta_2^2}}(K_0(p_2 e^{-iK_0 d} - q_2 e^{iK_0 d}))e^{i\nu}
\end{aligned} \tag{A11}$$

where $\nu = (n_2 - n_1)\phi_k/2 + \chi$ and we have assumed that $2\chi \ll K_0 d$. Thus we find that in this limit, the barrier potential once again appears as a constant shift in ϕ_k

as can be seen from expression of ν ; consequently, G becomes independent of χ if $n_2 \neq n_1$. Thus we expect to

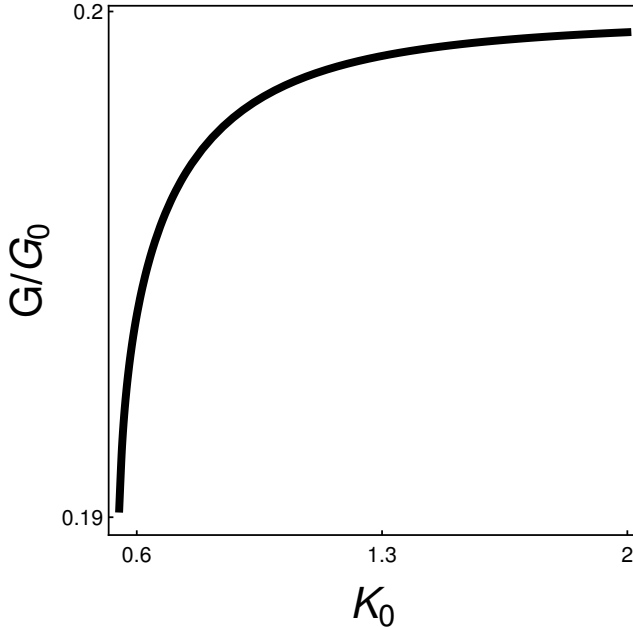


FIG. 10: Plot of the conductance G/G_0 as a function of K_0 (all momenta are in units of a). All parameters are same as in Fig. 9.

reproduce the results of the main text in this limit.

- ¹ B. Yan and C. Felser, *Ann. Rev. Cond. Mat* **8**, 337 (2017); M. Z. Hasan, S-Y Xu, I. Belopolski and S-M Huang, *ibid* **8**, 289 (2017); N.P Armitage, E.J. Mele, A. Vishwanath, *Rev. Mod. Phys.* **90**, 015001 (2018); A. A. Burkov, *Journal of Phys. Cond. Matt.* **27**, 113201 (2015); A. Turner and A. Vishwanath, arXiv:1301.0330 (unpublished); P. Hosur and X. Qi, *Comptes Rendus Physique*, **14**, 857 (2013); S.Rao, arXiv:1603.02821; W. Witczak-Krempa, G. Chen, Y. B. Kim, and L. Balents, *Annu. Rev. Condens. Matter Phys.* **5**, 57 (2014).
- ² X.G. Wan, A. M. Turner, A. Vishwanath A, S.Y Savrasov, *Phys. Rev. B* **83**, 205101 (2011); P. Hosur, S. A. Parameswaran and A. Vishwanath, *Phys. Rev. Lett.* **108**, 046602 (2012).
- ³ A. A. Burkov and L. Balents, *Phys. Rev. Lett.* **107**, 127205 (2011); A. A. Burkov, M. D. Hook and L. Balents, *Phys. Rev. B* **84**, 235126 (2011); G. Xu, H. Weng, Z. Wang, X. Dai, and Z. Fang, *Phys. Rev. Lett.* **107**, 186806 (2011); E-G Moon, C. Xu, Y B Kim, and L. Balents, *Phys. Rev. Lett.* **111**, 206401 (2013).
- ⁴ S. Y. Xu *et al.*, *Science* **349**, 613 (2015). B. Q. Lv *et al.*, *Phys. Rev. X* **5**, 031013 (2015).
- ⁵ A. A. Zyuzin and A. A. Burkov *Phys. Rev. B* **86**, 115133 (2012); M. N. Chernodub, A. Cortijo, A. G. Grushin, K. Landsteiner, and M. A. Vozmediano, *Phys. Rev. B* **89**, 081407 (2014); Z. Jian-Hui, J. Hua, N. Qian, and S. Jun-Ren, *Chin. Phys. Lett.* **30**, 027101 (2013); A. Burkov, *Journal of Physics: Condensed Matter* **27**, 113201 (2015); J. Ma, and D. A. Pesin, *Phys. Rev. B* **92**, 235205 (2015); S. Zhong, J. E. Moore, and I. Souza, *Phys. Rev. Lett.* **116**, 077201 (2016); A. Lucas, R. A. Davison, and S. Sachdev, *Proc. Natl. Acad. Sci. U.S.A.*, 201608881 (2016).
- ⁶ R. Wang, A. Go, and A. J. Millis, *Phys. Rev. B* **95**, 045133 (2017); D. Gosálbez-Martínez, I. Souza, and D. Vanderbilt, 2015, *Phys. Rev. B* **92**, 085138 (2015); P. Goswami, J. H. Pixley, and S. Das Sarma, *Phys. Rev. B* **92**, 075205 (2015).
- ⁷ A. G. Grushin, *Physical Review D* **86**, 045001 (2012); D. T. Son and N. Yamamoto, *Phys. Rev. Lett.* **109**, 181602 (2012); A. Zyuzin and A. Burkov, *Phys. Rev. B* **86**, 115133 (2012); A. Zyuzin, S. Wu, and A. Burkov, *Physical Review B* **85**, 165110 (2012).
- ⁸ L. Wu, M. Brahlé, R. V. Aguilar, A. Stier, C. Morris, Y. Lubashevsky, L. Bilbro, N. Bansal, S. Oh, and N. Armitage, *Nat. Phys.* **9**, 410 (2013); F.D.M Haldane, arXiv:1401.0529; I. Belopolski, *et al.*, *Phys. Rev. Lett.* **116**, 066802 (2016).
- ⁹ G. Xu, H. Weng, Z. Wang, X. Dai, and Z. Fang, *Phys. Rev. Lett.* **107**, 186806 (2011); Q. Liu and A. Zunger, *Phys. Rev. X* **7**, 021019 (2017).
- ¹⁰ C. Fang, M. J. Gilbert, X. Dai, and B. A. Bernevig, *Phys. Rev. Lett.* **108**, 266802 (2012); S.-M. Huang, S.-Y. Xu, I. Belopolski, C.-C. Lee, G. Chang, T.-R. Chang, *PNAC* **113**, 1180 (2016).
- ¹¹ C.-Z. Chen, J. Song, H. Jiang, Q.-f. Sun, Z. Wang, and X. C. Xie, *Phys. Rev. Lett.* **115**, 246603 (2015); P. Delplace, J. Li, and D. Carpentier, *Europhys. Lett.* **97**, 67004 (2012).
- ¹² Z-M Huang, J. Zhou, and S-Q Shen, arXiv:1705.04576.
- ¹³ S. Ahn, E.J. Mele, and H. Min, *Phys. Rev. B* **95**, 161112(R) (2017); L. Wang and S-K Jian, *Phys. Rev. B* **96**, 115448 (2017); S. P. Mukherjee and J. P. Carbotte, *Phys. Rev. B* **97**, 045150 (2018).
- ¹⁴ S. Ahn, E.H. Hwang, and H. Min, *Scientific Reports* **6**, 34023 (2016).
- ¹⁵ T. Hayata, Y. Kikuchi, and Y. Tanizaki, *Phys. Rev. B* **96**,

085112 (2017); Y. Sun and A. Wang, *Jour. Phys. Cond. Mat.* **29**, 435306 (2017); R. M. A. Dantas, F. Pena-Benitez, B. Roy, and P. Surowka, arXiv:1802.07733.

¹⁶ M. I. Katsnelson et al., *Nature Phys.* **2**, 620 (2006).

¹⁷ C. W. J. Beenakker, *Phys. Rev. Lett.* **97**, 067007 (2006).

¹⁸ S. Bhattacharjee and K. Sengupta, *Phys. Rev. Lett.* **97**, 217001 (2006); S. Bhattacharjee, M. Maiti and K. Sengupta, *Phys. Rev. B* **76**, 184514 (2007).

¹⁹ S. Mondal, D. Sen, K. Sengupta, and R. Shankar, *Phys. Rev. Lett.* **104**, 046403 (2010); *ibid* *Phys. Rev. B* **82**, 045120 (2010); A. R. Akhmerov, J. Nilsson, and C. W. J. Beenakker, *Phys. Rev. Lett.* **102**, 216404 (2009); Y. Tanaka, T. Yokoyama, and N. Nagaosa, *Phys. Rev. Lett.* **103**, 107002 (2009); J. Linder, Y. Tanaka, T. Yokoyama, A. Sudbo, and N. Nagaosa, *Phys. Rev. Lett.* **104**, 067001 (2010); T. Yokoyama, Y. Tanaka, and N. Nagaosa, *Phys. Rev. Lett.* **102**, 166801 (2009).

²⁰ C. W. J. Beenakker, *Rev. Mod. Phys.* **80**, 1337 (2008).

²¹ S. Ueda, T. Habe, and Y. Asano, *J. Phys. Soc. Jpn.* **83**, 064711 (2014); W. Chen, L. Jiang, R. Shen, L. Sheng, B. G. Wang, and D. Y. Xing, *Eur. Phys. Lett.* **103**, 27006 (2013).

²² K. A. Madsen, E. J. Bergholtz, and P. W. Brouwer, *Phys. Rev. B* **95**, 064511 (2017); N. Bovenzi, M. Breitkreiz, P. Baireuther, T. E. O'Brien, J. Tworzydo, I. Adagideli, and C. W. J. Beenakker, *Phys. Rev. B* **96**, 035437 (2017).

²³ S-B Zhang, F. Dolcini, D. Breunig, and B. Trauzettel, *Phys. Rev. B* **97**, 041116(R) (2018).

²⁴ D. K. Mukherjee, S. Rao and A. Kundu, *Phys. Rev. B* **96**, 161408(R) (2017); U. Khanna, A. Kundu and S. Rao, *Phys. Rev. B* **95**, 201115 (R) (2017); U. Khanna, D. K. Mukherjee, A. Kundu and S. Rao, *Phys. Rev. B* **93**, 121409 (R) (2016).

²⁵ B. Sbierski, G. Pohl, E. J. Bergholtz, and P. W. Brouwer, *Phys. Rev. Lett.* **113**, 026602 (2014); P. Hosur, S. A. Parameswaran, and A. Vishwanath, *Phys. Rev. Lett.* **108**, 046602 (2012).

²⁶ M. M. Fogler, F. Guinea, and M. I. Katsnelson, *Phys. Rev. Lett.* **101**, 226804 (2008).

²⁷ G. E. Blonder, M. Tinkham, and T. M. Klapwijk, *Phys. Rev. B* **25**, 4515 (1982).